# Solid-solution alloying of immiscible Pt and Au boosts catalytic performance for $H_2O_2$ direct synthesis

Hong Woo Lee [a,d,1], Hyobin Nam [b,c,1], Geun-Ho Han [d,1], Young-Hoon Cho [d], Byung Chul Yeo [a], Min-Cheol Kim [a], Donghun Kim [a,*], Kwan-Young Lee [d,*], Seung Yong Lee [b,c,*], Sang Soo Han [a,*]

[a] Computational Science Research Center, Korea Institute of Science and Technology, Seoul 02792, Republic of Korea
[b] Materials Achitecturing Research Center, Korea Institute of Science and Technology, Seoul 02792, Republic of Korea
[c] Department of Nanomaterials Science and Engineering, Korea University of Science and Technology, Daejeon 34113, Republic of Korea
[d] Department of Chemical and Biological Engineering, Korea University, Seoul 02841, Republic of Korea

A B S T R A C T

Here, we propose the solid-solution alloy nanoparticles (NPs) composed of Pt and Au supported on $TiO_2$ as an efficient catalyst for direct $H_2O_2$ synthesis, although Pt and Au are entirely immiscible in the bulk phases. Pt and Au atoms were homogeneously distributed in a wide composition range of $Pt_xAu_{100-x}$ NPs ($10 \leq x \leq 80$) supported on $TiO_2$. The most Au-rich $Pt_{10}Au_{90}$ NPs/$TiO_2$ exhibits the best catalytic performances, $H_2O_2$ selectivity ($94.5 \pm 0.6\%$) and productivity ($959 \pm 12$ $mmol_{H2O2} \cdot g_{metal}^{-1} \cdot h^{-1}$), even under mild conditions (10 °C, 1 atm) and without halide-ion additives. Density functional theory calculations reveal that the introduction of inactive Au atoms strongly suppresses both O-O bond scission and OH hydrogenation, thereby enabling near unity selectivity. The Pt-Au catalyst is Pd-absent, which is noteworthy given previous efforts in direct $H_2O_2$ synthesis are mostly limited to prototypical Pd or Pd-based modifications. This work will stimulate active utilization of immiscible elemental combinations for the direct $H_2O_2$ synthesis catalyst development.

© 2020 Acta Materialia Inc. Published by Elsevier Ltd. All rights reserved.

## 1. Introduction

Hydrogen peroxide ($H_2O_2$) is well known as an eco-friendly oxidizing agent and is used for disinfection and bleaching in the pulp and paper industries [1]. Currently, it is mainly produced by the sequential hydrogenation and auto-oxidation of anthraquinone (AQ) [2], which is called indirect synthesis. However, this process is energy intensive and requires large-scale facilities; additionally, AQ is toxic. To circumvent such issues, direct synthesis of $H_2O_2$ from molecular $H_2$ and $O_2$ can be considered a promising alternative [3–5].

Palladium (Pd) has been regarded as an archetypical catalyst for direct $H_2O_2$ synthesis [4], although there is still much room for the performance enhancement. To improve its catalytic performance, the metallic alloying approach has extensively been used; those efforts, however, have been mainly limited to Pd-based modifications thus far [2,6–13]. Examples include Pd-Au [2,6–8], Pd-Ni [9,10], and Pd-Sn [11] systems, which have shown markedly en-

hanced catalytic performances for $H_2O_2$ production. Importantly, we witness in these studies that the reported elemental combinations are all thermodynamically miscible in the bulk phase, with negative bulk-formation energies. In these cases, the two elements tend to be homogeneously mixed at the atomic level. On the other hand, bulk-immiscible elements (with positive formation energy) have been thoroughly disregarded in bimetallic catalysis for $H_2O_2$ synthesis mainly because of the inherent difficulty of alloy synthesis (phase separations).

Nonequilibrium phases can be stabilized by a nanosize effect. Indeed, various nonequilibrium solid-solution alloy nanoparticles (NPs) of Pd-Ru [14], Pd-Rh [15], Au-Ni [16], Cu-Rh [17], Cu-Rh [18], and Rh-Ag [19] have successfully been synthesized, although these elemental combinations are all immiscible in the bulk phase. In this study, we focus on NPs composed of Pt and Au. Given that catalysts for $H_2O_2$ direct synthesis should desirably offer sites for both H-H bond scission and O-O bond preservation, we selected Pt and Au, which are the best-known elements to satisfy each requirement [20–22]. Thus, we hypothesize that a solid-solution alloying of Pt and Au would possibly provide a positive synergy in $H_2O_2$ production, although each element alone cannot serve as an effective catalyst.

---

* Corresponding author.
   E-mail addresses: donghun@kist.re.kr (D. Kim), kylee@korea.ac.kr (K.-Y. Lee), patra@kist.re.kr (S.Y. Lee), sangsoo@kist.re.kr (S.S. Han).
[1] These authors contributed equally to this work.

Here, using a joint theoretical-experimental study, we report the successful synthesis of solid-solution $Pt_xAu_{100-x}$ NPs supported on $TiO_2$ over a wide composition range ($10 \leq x \leq 80$), although Pt and Au are immiscible in the bulk phase. The most Au-rich $Pt_{10}Au_{90}$ NPs/$TiO_2$ provided the best catalytic performance in terms of both selectivity ($94.5 \pm 0.6\%$) and productivity ($958 \pm 12$ $mmol_{H2O2} \cdot g_{metal}^{-1} \cdot h^{-1}$), even under mild conditions (10 °C, 1 atm) and without halide-ion additives. As the price of Pd has rapidly increased, we find that the Pd-free PtAu NPs can serve as a more cost-effective option. Moreover, this catalyst is stable for a long time ($>8$ h). Density functional theory (DFT) calculations reveal that both O-O bond scission and OH hydrogenation, leading to generation of $H_2O$, are strongly suppressed for the Au-rich samples (Au$>75\%$), which adequately explains the near-unity selectivity in experiments. The present work is, to our knowledge, the first demonstration of stabilizing nonequilibrium solid-solution NPs for $H_2O_2$ synthesis, thus stimulating the active utilization of other bulk-immiscible elements for catalyst development in the future.

## 2. Experimental and calculation methods

### 2.1. Chemicals

Poly(vinylpyrrolidone) (PVP, MW = 55,000), gold(III) chloride trihydrate [$HAuCl_4 \bullet 3H_2O$, 99.9%], chloroplatinic acid hydrate [$H_2Cl_6Pt \bullet XH_2O$, ~38%], palladium(II) nitrate dihydrate ($Pd(NO_3)_2 \cdot 2H_2O$, Sigma-Aldrich), and sodium borohydride [$NaBH_4$, 98%] were purchased from Sigma-Aldrich. Titanium dioxide ($TiO_2$, P25) was purchased from Degussa. All solvents, including deionized water (18.2 MΩ•cm), ethanol ($C_2H_6O$, ≥99.5%, Sigma-Aldrich), hydrochloric acid (HCl, 37%, Sigma-Aldrich), sulfuric acid ($H_2SO_4$, 99.999%, Sigma-Aldrich) and hydrogen peroxide ($H_2O_2$, 35 wt.% in $H_2O$, Sigma-Aldrich) were used without further purification.

### 2.2. Catalyst synthesis

Pt-Au nanoparticles were synthesized using a gold(III) chloride trihydrate and chloroplatinic acid hydrate solution. A total of 153 mg of PVP, 23 mg of $NaBH_4$ and 30 mg of $TiO_2$ were dispersed in 15 mL of deionized water. Furthermore, Pt and Au metal precursors of 0.01 mmol in total were dissolved in 5 mL of deionized water. The aqueous solution containing Pt and Au precursors was added dropwise to deionized water containing PVP and $NaBH_4$ in an ice-water bath. The resulting catalyst NPs were collected by centrifugation (12,000 rpm) and then washed with DI water two times to remove excess PVP. A schematic illustration of the Pt-Au preparation process is shown in Scheme S1 in the supporting materials. Pd/$TiO_2$ catalysts were prepared by an incipient wetness impregnation method [23] and used as a reference for comparisons with the Pt-Au catalysts in this work. Palladium(II) nitrate dihydrate (25 mg) was dissolved in 0.25 mL of deionized water. The obtained precursor solution was then dropped on 1 g of titanium dioxide for metal impregnation according to the general incipient wetness impregnation technique [23]. Then, the powder was dried at 110 °C for 12 h before calcination at 500 °C for 3 h with a heating rate of 2 °C/min. The Pd/$TiO_2$ was reduced using a $H_2/N_2$ gas mixture (1:9 volume ratio) at 150 °C for 1.5 h.

### 2.3. Catalyst characterizations

Transmission electron microscopy (TEM) images and energy–dispersive X–ray spectra (EDS) were acquired using a transmission electron microscope (FEI Talos F200X) equipped with scanning transmission electron microscopy–energy dispersive X–ray spectroscopy (Bruker Super–X EDS system). The crystal structure was examined by X–ray diffraction (Rigaku Dmax 2500 and Smartlab)

with Cu K$\alpha$ radiation ($\lambda$ = 1.54 Å). The samples for the TEM images and XRD spectra were purified by centrifugation three times to remove the surfactants and/or excess reactants. Then, the NPs were dispersed in ethanol. The resulting dispersion was dropped on a copper grid coated with an amorphous carbon film for the TEM images and on a soda-lime-silica glass for the XRD spectra. The actual compositions of each alloy catalyst were measured via inductively coupled plasma mass emission spectrometry (ICP-MS) using a NexION 350D (Perkin-Elmer, USA). The electronic structures were characterized with X-ray photoelectron spectroscopy (XPS, Thermo VG Scientific K-alpha, Al Kα).

### 2.4. Catalytic performance measurements

The catalytic direct $H_2O_2$ synthesis reaction and $H_2O_2$ hydrogenation test were performed in a double-jacketed glass reactor under continuous stirring at 1200 rpm. For $H_2O_2$ synthesis, the reaction medium (total of 60 mL) consisted of ethanol with $1.5 \times 10^{-1}$ M $H_2SO_4$ and $4.0 \times 10^{-4}$ M HCl. The weight of the PtAu metal was fixed at 0.5 mg. The flow rate of the reactant gas stream was 20 mL/min (volumetric ratio of $H_2$:$O_2$ = 1:24), and the reaction was performed at 10 °C and 1 atm for 1 h. In the $H_2O_2$ hydrogenation test, reactions were performed using 20 $\mu$L of $H_2O_2$ (30 wt.% in $H_2O$, Sigma-Aldrich) in solvent (60 mL of ethanol containing $1.5 \times 10^{-1}$ M $H_2SO_4$ and $4.0 \times 10^{-4}$ M HCl). The flow rate of the reactant gas stream was 20 mL/min (volumetric ratio of $H_2$:$N_2$ = 1:24) and the reaction was performed at 10 °C and 1 atm for 1 h. After the reaction, the $H_2$ conversion was measured using gas chromatography (GC). The $H_2O_2$ concentration was measured using the iodometric titration method. The $H_2O_2$ selectivity was calculated by using the quantity of converted $H_2$ (GC) and the quantity of produced $H_2O_2$ (titration).

### 2.5. Computational details

All DFT calculations were performed using the Vienna Ab Initio Simulation Packages (VASP) [24] using the projector-augmented-wave (PAW) [25] method to describe the potential from the ionic core. For the exchange and correlation terms, we employed the revised Perdew-Burke-Ernzerhof (RPBE) functional [26]. An energy cut-off of 480 eV and Monkhorst-Pack k-point meshes of $8 \times 8 \times 8$ and $3 \times 3 \times 1$ for the bulk and slab calculations, respectively, were used after an extensive convergence test. A large vacuum spacing of 15 Å was used to prevent interslab interactions. Each (111) surface was modeled by a supercell slab that consisted of a $4 \times 4$ surface unit cell with four layers for direct synthesis and a $4 \times 6$ surface unit cell with three layers for $H_2O_2$ hydrogenation. The top two layers and the reactant molecules were optimized until the energy change was less than $1 \times 10^{-4}$ eV/cell and the force on each atom was less than 0.02 eV Å$^{-1}$. In addition, the nudged elastic band (NEB) [27] method was employed to investigate the transition state for each reaction on the Pt-Au system.

## 3. Results and discussion

### 3.1. Synthesis and characterization of solid-solution Pt-Au NPs supported over $TiO_2$ (Pt-Au NPs/$TiO_2$)

Bimetallic Pt-Au NPs/$TiO_2$ were synthesized by a chemical reduction method using $NaBH_4$ solution. By varying the ratio of Pt and Au precursors (loading ratio of Pt:Au = 90:10, 70:30, 50:50, 30:70, and 10:90), we obtained five Pt-Au NPs with different compositions ($Pt_xAu_{100-x}$). Inductively coupled plasma (ICP) analysis revealed that the actual compositions of the synthesized Pt-Au NPs were $Pt_{80}Au_{20}$, $Pt_{65}Au_{35}$, $Pt_{44}Au_{56}$, $Pt_{27}Au_{73}$, and $Pt_{10}Au_{90}$.
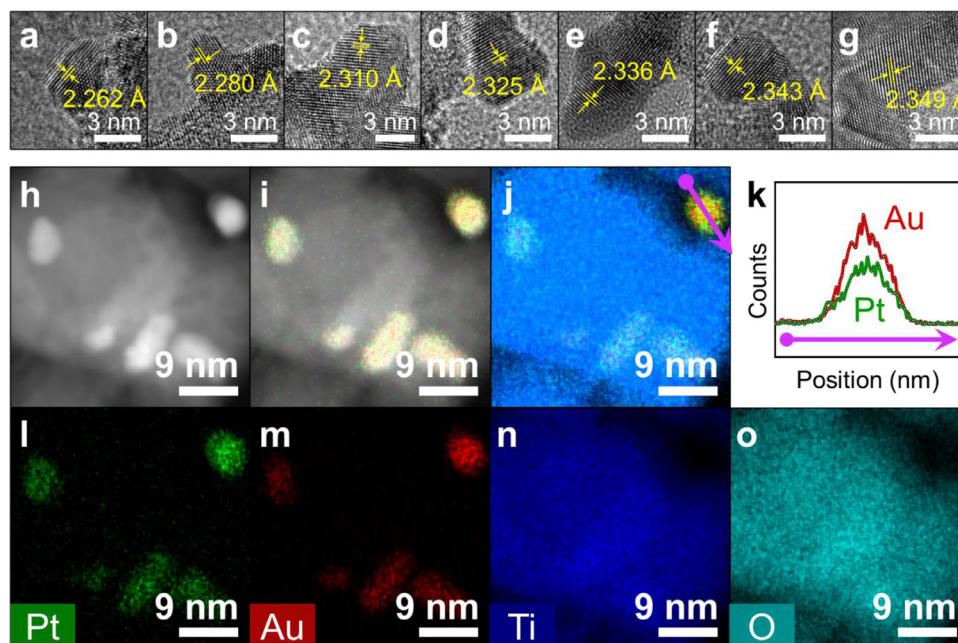
**Fig. 1.** Characterizations of $Pt_xAu_{100-x}$ NPs/$TiO_2$. **a-g,** HRTEM images of $Pt_{100}$ (**a**), $Pt_{80}Au_{20}$ (**b**), $Pt_{65}Au_{35}$ (**c**), $Pt_{44}Au_{56}$ (**d**), $Pt_{27}Au_{73}$ (**e**), $Pt_{10}Au_{90}$ (**f**) and $Au_{100}$ (**g**). **h,** grayscale HAADF image. **i-o,** STEM-EDS color mapping analysis of the $Pt_{44}Au_{56}$ NPs. Color maps of Pt-L STEM-EDS in green (**l**), Au-L STEM-EDS in red (**m**), Ti-K STEM-EDS in blue (**n**), O-K STEM-EDS in cyan (**o**), the overlay of Pt/Au (**i**), and the overlay of all elements (**j**). **k,** the line scan profiles of Pt and Au along the arrow shown in (**j**).
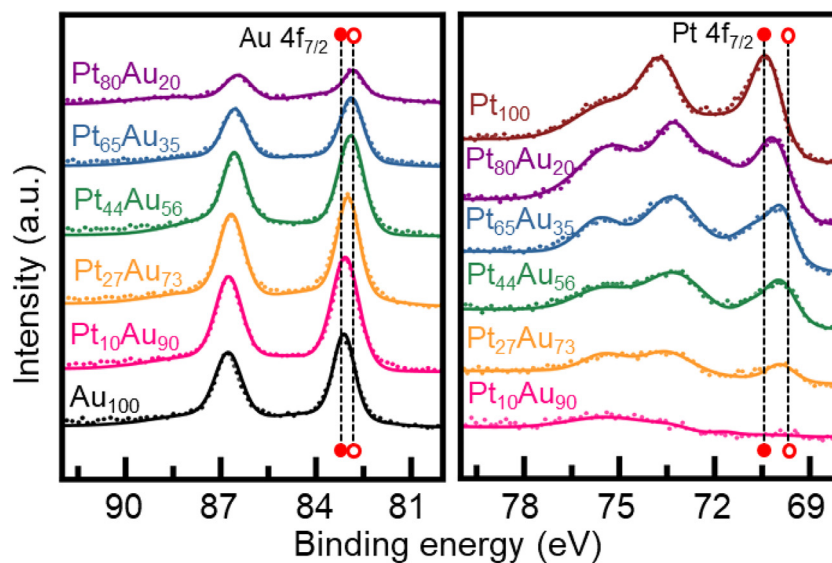


**Fig. 2.** X-ray photoelectron spectroscopy (XPS) analysis of $Pt_xAu_{100-x}$ NPs/$TiO_2$ over wide compositions. Vertical dotted-lines terminated by closed red circles in each panel indicate the peak positions of Au $4f_{7/2}$ of pure Au ($Au_{100}$) and Pt$4f_{7/2}$ of pure Pt ($Pt_{100}$), respectively. Vertical dotted-lines terminated by closed red circles in each panel indicate the peak positions of Au $4f_{7/2}$ of pure Au ($Au_{100}$) and Pt$4f_{7/2}$ of pure Pt ($Pt_{100}$), respectively. Vertical dotted-lines terminated by open red circles indicate the peak position of the Au $4f_{7/2}$ of $Pt_{80}Au_{20}$ NPs and Pt $4f_{7/2}$ of $Pt_{10}Au_{90}$ NPs.

A series of spectroscopies were applied to study these $Pt_xAu_{100-x}$ NPs to provide evidence of solid-solution alloying of Pt and Au. In Fig. 1a-g, the high-resolution transmission electron microscopy (HRTEM) reveals the change in lattice parameters with varying compositions. Due to face-centered cubic (FCC) structures, (111) planes are clearly observed. The interplanar distances between the (111) planes monotonically increase with increasing Au content from 2.262 Å for pure Pt to 2.349 Å for pure Au, which supports the alloying states of Pt and Au on an atomic scale.

As shown in Fig. 1h-o, energy dispersive X-ray spectra (EDS) analysis was performed. The $Pt_{44}Au_{56}$ NPs/$TiO_2$ sample is shown as a representative, although other compositional cases are all available in Figs. S2. The elemental color mappings of Pt, Au, Ti, and

O and their overlay clearly confirm the settlement of nanoparticles on the $TiO_2$ support, and indicate the homogeneous mixing of Pt and Au atoms in each particle. The EDS line scan profile (Fig. 1k) passing through the NP center reveals that the Pt and Au atoms are homogenously distributed, as seen by the uniform atomic ratio at any part of the NPs. This is similarly observed for other compositional cases (Fig. S4). In addition, we confirmed with TEM (Fig. S6) and STEM-EDS (Fig. S7) techniques that the Pt-Au NPs were well supported on $TiO_2$.

In Fig. 2, X-ray photoelectron spectroscopy (XPS) analysis was also performed to understand the charge redistribution state of each Pt and Au element. We first note that, for pure Pt and Au NPs, the metallic Pt and Au $4f_{7/2}$ peaks appear at approximately 70.5 eV

and 83.0 eV, both of which are smaller by 1.0–1.5 eV relative to the reference peak positions of Pt and Au 4f that are unaffected by any support or impurities. These disparities in binding energy likely originate from the electron transfer occurring from the $TiO_2$ support to NPs, as similarly reported in other works [28–31]. In the case of $Pt_xAu_{100-x}$ alloys, while the metallic Au peaks are steadily shifted toward the lower binding energy by as much as 0.15 eV upon increasing the Pt content, the metallic Pt peaks shift in the opposite direction up to 0.6 eV. These monotonic trends in peak shifts indicate that the electrons gradually transfer from Pt to Au within NPs, which is also supportive evidence of the homogeneous Pt-Au mixing states [31].

The combined study using HADDF-STEM, EDS, and XPS techniques consistently characterizes the solid-solution alloying of Pt and Au in $Pt_xAu_{100-x}$ NPs/$TiO_2$. We would like to briefly explain the omission of the most basic X-ray diffraction (XRD) data. We found that the XRD analysis of $Pt_xAu_{100-x}$ NPs/$TiO_2$ was extremely difficult due to the overlap of peaks between the NPs and $TiO_2$ supports (Fig. S1); thus, the data are omitted in the main text. However, the XRD analysis of Pt-Au NPs alone (excluding $TiO_2$), which was produced by similar synthetic procedures but without Ti precursors, showed diffraction patterns consistent with single face-centered cubic (fcc) structures with no signals from pure Pt and Au phases, which was also supported by our simulations (Fig. S8). The diffraction peaks of the Pt-Au NPs shifted continuously toward lower angles with increasing Au content, which though indirect, supports the formation of the solid-solution Pt and Au alloy.

### 3.2. Catalytic performances of the Pt-Au NPs/$TiO_2$

The catalysts for solid-solution $Pt_xAu_{100-x}$ NPs/$TiO_2$ were tested for direct $H_2O_2$ synthesis under mild reaction conditions (10 °C, 1 atm) and with no halide-ion additives, in comparison to pure Pt, Au, and Pd. In Table 1, we first observe that for $Pt_xAu_{100-x}$ NPs, $H_2$ conversions gradually decreased (53.3% → 23.7%) with increasing Au content (20% → 90%), consistent with the tendency of Au not to dissociate $H_2$ molecules [32]. However, even the most Au-rich $Pt_{10}Au_{90}$ NPs exhibit a $H_2$ conversion of 23.7% (higher than 12.3% of pure Pd), owing to the strong $H_2$ dissociative nature of Pt.

The $Pt_xAu_{100-x}$ NPs/$TiO_2$ exhibit a substantially enhanced $H_2O_2$ productivity compared to pure Pt and Au NPs. Both productivity and selectivity increase with increasing Au content, and the best values for both are achieved at Au contents of 90% ($Pt_{10}Au_{90}$ NPs) of $959 \pm 11$ $mmol_{H2O2} \cdot g_{metal}^{-1} \cdot h^{-1}$ and $94.5 \pm 0.7\%$, respectively. These values are much higher than those of the archetypical Pd ($417 \pm 11$ $mmol_{H2O2} \cdot g_{metal}^{-1} \cdot h^{-1}$, 79.7%). In Table S2, catalytic properties of Pd-Au catalysts, the known best catalysts for $H_2O_2$

synthesis, are also shown for comparisons. Because each reaction in development for the $H_2O_2$ direct synthesis was not performed under the same conditions including reactor type, additive, and pressure etc., such comparison could be indirect. However, it can be more direct comparison by comparing of $H_2O_2$ selectivity, because the selectivity can be measured from the amount of $H_2O_2$-generated compared to the initial input amount of $H_2$. The comparison in the table reveals that Pt-Au catalyst has a high $H_2O_2$ selectivity even in ambient conditions.

As $H_2$ conversions are much different across samples (in our case, ranging from 12.3% for Pd to 53.5% for $Pt_{80}Au_{20}$), experiments under isoconversion conditions are also performed for an accurate performance comparison (Table S4). At the controlled $H_2$ conversion level close to 24%, $Pt_{10}Au_{90}$ NPs still greatly outperform all other samples, and notably the performance gaps with pure Pd become even larger. It is impressive that Au alone is completely inactive for $H_2O_2$ synthesis while a highly Au-rich sample ($Pt_{10}Au_{90}$ NPs) can be extremely active.

The Pt-Au catalysts become more attractive relative to Pd in another productivity metric, i.e., the cost-normalized productivity (CNP; unit, $mmol \cdot \$_{metal}^{-1} \cdot h^{-1}$) of the Pt-Au catalysts. CNP is the $H_2O_2$ productivity based on the metal price of U.S. dollar ($) instead of catalyst mass (g), and is thus more appropriate in evaluating the cost effectiveness. The $Pt_{10}Au_{90}$ NPs exhibit the highest CNP value of 19.6 $mmol \cdot \$_{metal}^{-1} \cdot h^{-1}$ among the tested samples, which is 3.6 times higher than the value of 5.5 $mmol \cdot \$_{metal}^{-1} \cdot h^{-1}$ for pure Pd. This price competitiveness results from the fact that Pd is 3.2-fold and 1.5-fold more expensive than Pt and Au, respectively [33].

Usually, catalysts for $H_2O_2$ direct synthesis are also effective for the sequential hydrogenation and/or decomposition of $H_2O_2$ to water ($H_2O$) [11,12,34–37], and thus it is critical to stabilize $H_2O_2$ produced on the catalysts to maintain a high performance. To present additional evidence of the superior selectivity of Pt-Au NPs (as high as 94.5% for $Pt_{10}Au_{90}$), $H_2O_2$ hydrogenation tests were performed under the same reaction conditions of 10 °C and 1 atm (Table 1). We observe that the $H_2O_2$ hydrogenation rate drastically drops with increasing Au content, and thus the $Pt_{10}Au_{90}$ NPs exhibit the lowest $H_2O_2$ hydrogenation rate (384 $mmol_{H2O2} \cdot g_{metal}^{-1} \cdot h^{-1}$) compared to other Pt-Au samples as well as Pd NPs (805 $mmol_{H2O2} \cdot g_{metal}^{-1} \cdot h^{-1}$). After 1 h of reaction, only 1.2% of the input $H_2O_2$ was consumed and transformed into water for $Pt_{10}Au_{90}$ NPs, while 24.6% and 2.5% of $H_2O_2$ were hydrogenated on the pure Pt and Pd, respectively. The relatively stronger resistance to $H_2O_2$ degradation for $Pt_{10}Au_{90}$ NPs supports the observed exceptional $H_2O_2$ selectivity.

**Table 1**
Catalytic performances of Pt-Au NPs in comparison to those of pure Pd, Pt and Au NPs.

| Catalyst | $H_2O_2$ synthesis | | | | $H_2O_2$ hydrogenation | |
| | $H_2$ conversion (%) | $H_2O_2$ selectivity (%) | $H_2O_2$ productivity | | Rate ($mmol_{H2O2}$ $\cdot g_{metal}^{-1} \cdot h^{-1}$) | Percentage of $H_2O_2$ consumption (%) |
| | | | Mass-normalized ($mmol_{H2O2} \cdot g_{metal}^{-1} \cdot h^{-1}$) | Cost-normalized ($mmol_{H2O2} \cdot \$_{metal}^{-1} \cdot h^{-1}$) | | |
|---|---|---|---|---|---|---|
| Pd | 12.3 (±0.4) | 79.7 (±0.5) | 417 (±11) | 5.5 | 805 | 2.5 |
| Pt | 52.1 (±0.4) | 10.9 (±1.6) | 240 (±33) | 10.3 | 8,061 | 24.6 |
| Au | 0 | 0 | 0 | 0 | 184 | 0.8 |
| $Pt_{80}Au_{20}$ | 53.3 (±0.4) | 18.7 (±0.6) | 425 (±11) | 14.6 | 6,207 | 19.0 |
| $Pt_{65}Au_{35}$ | 50.0 (±0.8) | 21.7 (±0.1) | 462 (±5) | 13.9 | 5,079 | 15.5 |
| $Pt_{44}Au_{56}$ | 43.5 (±1.0) | 39.4 (±0.3) | 725 (±10) | 18.5 | 2,421 | 7.4 |
| $Pt_{27}Au_{73}$ | 30.8 (±1.1) | 67.9 (±2.6) | 856 (±24) | 19.4 | 899 | 2.7 |
| $Pt_{10}Au_{90}$ | 23.7 (±0.1) | 94.5 (±0.7) | 959 (±11) | 19.6 | 384 | 1.2 |

The $H_2O_2$ synthesis reactions were carried out under the following conditions: temperature, 10 °C; pressure, 1 atm; reaction medium, a total of 60 mL of ethanol with $1.5 \times 10^{-1}$ M $H_2SO_4$ and $4.0 \times 10^{-4}$ M HCl; used metal weight, 0.5 mg; flow rate, 20 mL/min; $H_2/O_2$=1/24. The $H_2O_2$ hydrogenation reactions were performed under the following conditions (not stated if same as $H_2O_2$ synthesis case): the loading volume of $H_2O_2$, 20 $\mu$L (30 wt.% in $H_2O$, Sigma-Aldrich); flow rate, 20 mL; $H_2/N_2$=1/24. The percentage of $H_2O_2$ consumption was measured at 1hr hydrogenation reaction. Both reactions were performed in a double-jacketed glass reactor under continuous stirring at 1200 rpm for 1 h. All catalysts were supported on $TiO_2$.
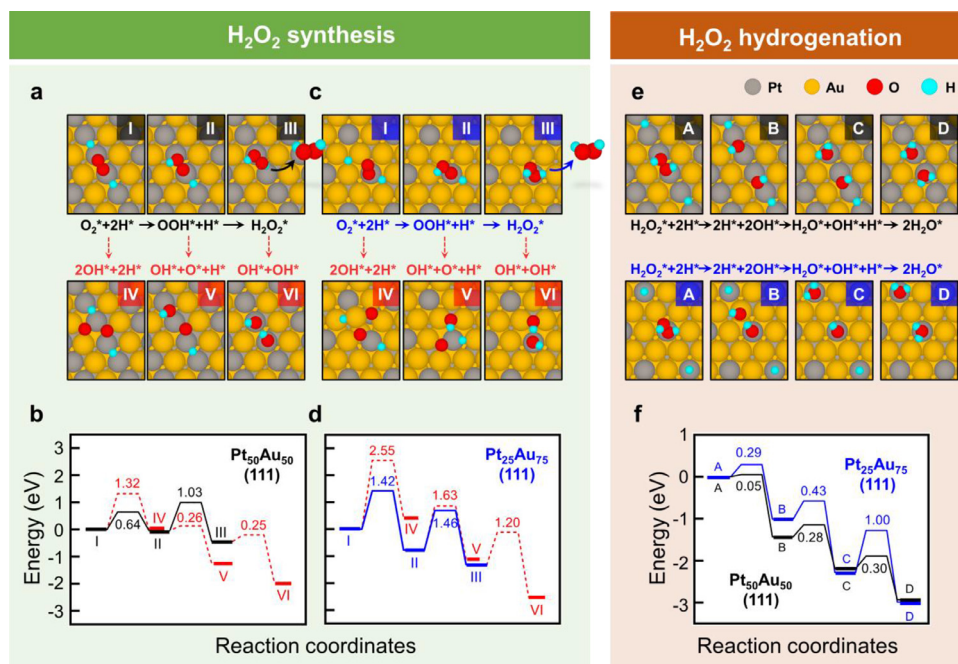
**Fig. 3. DFT modeling results of H₂O₂ synthesis and hydrogenation. a-d,** $H_2O_2$ synthesis mechanisms. Optimized structures and corresponding reaction energetics (both main and side reactions) for $Pt_{50}Au_{50}(111)$ (**a, b**) and $Pt_{25}Au_{75}(111)$ (**c, d**). **e-f,** $H_2O_2$ hydrogenation mechanisms. Optimized structures (**e**) and corresponding energetics (**f**) for each $Pt_{50}Au_{50}(111)$ and $Pt_{25}Au_{75}(111)$. The values written in the energetics graphs (**b,d,f**) represent the activation energy barrier of each reaction step.

### 3.3. H₂O₂ synthesis and hydrogenation mechanisms determined by DFT calculations

To understand the origins of the superior catalytic performance of the Au-rich Pt-Au alloys, we explored the reaction mechanisms of $H_2O_2$ synthesis using DFT calculations (Fig. 3a–d). We considered close-packed (111) surfaces of $Pt_{50}Au_{50}$ and $Pt_{25}Au_{75}$ slabs in the $L1_0$ and $L1_2$ phases, respectively, after surface energy comparisons between low index facets of (111), (110) and (100) (Table S5), in which the atomic structures were also supported by DFT calculations (Fig. S8c). The initial positions of both $H_2^*$ and $O_2^*$ species (* indicates surface sites) were determined after extensive adsorption energy calculations over various most-likely geometries in the unit cell (Figs. S9-S11 and Table S6). For both the $Pt_{50}Au_{50}$ and $Pt_{25}Au_{75}$ surfaces, $H_2$ molecules prefer sitting on top of Pt atoms and are immediately dissociated into H atoms due to a very small barrier of 0.02 eV (close to room temperature thermal energy of 26 meV). This energy barrier is smaller than that of Pd(111) (0.22 eV) [20], which adequately explains the generally larger $H_2$ conversion values of Pt-Au NPs regardless of the composition relative to Pd NPs (Table 1).

In Fig. 3a and b, starting with $Pt_{50}Au_{50}(111)$, the overall $H_2O_2$ synthesis involving two sequential hydrogenations (I→II and II→III) is exothermic by -0.44 eV, while the same process is endothermic for Pd(111) [20]. This explains the higher $H_2O_2$ production rate of $Pt_{44}Au_{56}$ NPs (the closest composition in our experiments) than that of Pd NPs (Table 1). We observe for $Pt_{50}Au_{50}(111)$ that the first side reaction ($O_2^*$ dissociation; I→IV) is well suppressed, with a high energy barrier of 1.32 eV; however, the second side reaction (OOH* dissociation; II→V) can occur favorably. This feature is not beneficial to $H_2O_2$ selectivity, and is likely responsible for the <40% selectivity of $Pt_{44}Au_{56}$ NPs.

In Fig. 3c and d, to explain the improved performance of Au-rich Pt-Au samples, the reaction energetics over $Pt_{25}Au_{75}(111)$ are presented. The overall $H_2O_2$ production (I→III) is greatly exothermic, by 1.31 eV. More importantly, the side reactions at both hydrogenation steps (I→IV and II→V) are well suppressed, as both

barriers are determined to be higher than those of the main reactions. This feature is not observed for the $Pt_{50}Au_{50}(111)$ surface and well explains the observed increasing trend in productivity and selectivity at higher Au contents. Although we did not carry out a simulation of a highly Au-rich case (for example, an Au composition of ~90% in experiments), we find in Fig. S16 that $O_2$ dissociation energetics dramatically turn at Au > 75% from exo- to endothermic reactions. We speculate that such strong $O_2$ bond-preserving nature of Au maximally synergizes with the favorable $H_2$-dissociating nature of Pt at the composition of Pt:Au=1:9, which can be expected from the fact that $H_2$ dissociation can readily occur even over Pt single atoms surrounded by Au atoms (Fig. S15).

In Fig. 3e and f, to assess the stability of the produced $H_2O_2$ species, the $H_2O_2$ hydrogenation behaviors are additionally investigated. The most prominent difference between the $Pt_{50}Au_{50}(111)$ and $Pt_{25}Au_{75}(111)$ surfaces is at the energy barriers. While the barriers in the water formation path (A→B→C→D) are all lower than 0.30 eV for $Pt_{50}Au_{50}$, these are as high as 1.00 eV (C→D; OH hydrogenation) for the $Pt_{25}Au_{75}$ slab. We find that this high barrier for OH hydrogenation originates from limited hydrogen diffusion. H atoms prefer sitting on top of Pt; however, their diffusion toward OH species is mandatory to complete the water formation process. For samples with high Au contents (Au>75%), Pt atoms are most likely distributed in an isolated manner, which makes hydrogen diffusion extremely difficult. This prevents the $H_2O_2$ species from being transformed into water and consequently explains the decreasing trend in $H_2O_2$ hydrogenation rates for high Au-content NPs ($Pt_{27}Au_{73}$ and $Pt_{10}Au_{90}$ NPs in Table 1).

### 3.4. Long-term stability

To warrant sustainable $H_2O_2$ production over time, the long-term stability has also been taken into account. The best catalyst of $Pt_{10}Au_{90}/TiO_2$ was selected for the stability investigations.

Fig. 4a shows the accumulated concentration of $H_2O_2$ over 8 h for $Pt_{10}Au_{90}/TiO_2$ as well as $Pd/TiO_2$ as a comparison. Our catalyst is fairly stable over time: the concentration for $Pt_{10}Au_{90}/TiO_2$
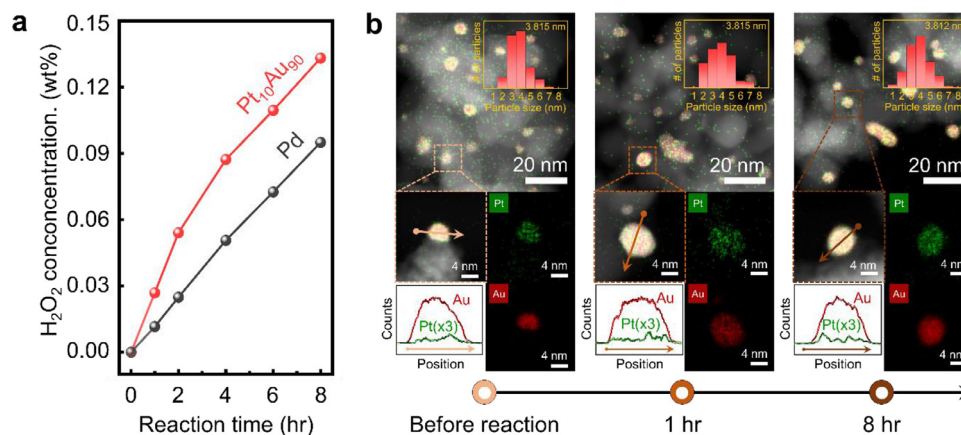
**Fig. 4.** **Long-term stability of $Pt_{10}Au_{90}$ NPs/$TiO_2$. a,** Accumulated $H_2O_2$ concentration of $Pt_{10}Au_{90}$ NPs/$TiO_2$ over time (up to 8 h) in a comparison to Pd NPs/$TiO_2$. **b,** TEM-EDS color mapping analysis of $Pt_{10}Au_{90}$ NPs after 0, 1, and 8 h of reaction. Color maps of Pt-L STEM-EDX in green, Au-L STEM-EDX in red, and their overlay are shown. The line scan profiles are shown for each representative NP. The insets show the size distribution histograms of particle diameters at each time.

monotonically increases, reaching 0.13 wt.% at 8 h, which is larger than 0.09 wt.% of Pd/$TiO_2$. The morphology of the $Pt_{10}Au_{90}$ NPs barely changed even after the long-term reactions. In Fig. 4b, the TEM-EDS analysis results are shown for the $Pt_{10}Au_{90}$ NPs/$TiO_2$ sample after 0, 1, and 8 h of reactions. The size distribution histograms of the NP diameters remain largely unchanged (3.81–3.82 nm on average). The EDS maps of each Pt and Au, as well as the line scan profiles, reveal that the homogeneous mixing state is preserved within NPs. This characterization supports the strong morphological stability of catalyst materials in the reaction medium. This also addresses our concern that the solid-solution alloyed Pt-Au NPs may be transformed into phase-separated NPs over time due to their inherent immiscibility.

## 4. Conclusion

In developing a novel bimetallic alloy catalyst, an immiscible elemental combination has thoroughly been disregarded due to the inherent difficulty of the alloying process. In this work, we report solid-solution Pt-Au alloy NPs supported on $TiO_2$ as an efficient catalyst for direct synthesis of $H_2O_2$, although Pt and Au are entirely immiscible in the bulk phase. A combined analysis based on STEM, EDS and XPS reveals that Pt and Au are indeed homogeneously mixed at an atomic level in various compositional Pt-Au samples, i.e., $Pt_xAu_{100-x}$ with $10{\leq}x{\leq}80$. The most Au-rich $Pt_{10}Au_{90}$/$TiO_2$ performs the best, with $H_2O_2$ production rates ($959 \pm 12$ $mmol_{H2O2}{\cdot}g_{metal}^{-1}{\cdot}h^{-1}$) and selectivity ($94.5 \pm 0.6\%$) even under mild conditions (10 °C, 1 atm) and without halide-ion additives, greatly exceeding those of the prototypical Pd. DFT calculations reveal that the introduction of inactive Au atoms strongly suppresses both O-O bond scission and OH hydrogenation, thereby enabling near unity selectivity. In addition to proposing an efficient catalyst, this work will turn our attention to the promise of the overlooked class of immiscible elemental combinations for catalyst development.

## Declaration of Competing Interest

The authors declare that they have no known competing financial interests or personal relationships that could have appeared to influence the work reported in this paper.

## Acknowledgment

## Supplementary materials

Supplementary material associated with this article can be found, in the online version, at doi:10.1016/j.actamat.2020.116563.

## References

[1] P.B. Walsh, Hydrogen peroxide: innovations in chemical pulp bleaching, Tappi. J. 74 (1991) 81–83.

[2] J.K. Edwards, G.J. Hutchings, Palladium and gold–palladium catalysts for the direct synthesis of hydrogen peroxide, Angew. Chem. Int. Edit. 47 (2008) 9192–9198.

[3] D.P. Dissanayake, J.H. Lunsford, Evidence for the role of colloidal palladium in the catalytic formation of $H_2O_2$ from $H_2$ and $O_2$, J. Catal. 206 (2002) 173–176.

[4] J.H. Lunsford, The direct formation of $H_2O_2$ from $H_2$ and $O_2$ over palladium catalysts, J. Catal. 216 (2003) 455–460.

[5] Y.F. Han, J.H. Lunsford, Direct formation of $H_2O_2$ from $H_2$ and $O_2$ over a Pd/$SiO_2$ catalyst: the roles of the acid and the liquid phase, J. Catal. 230 (2005) 313–316.

[6] J.K. Edwards, B. Solsona, E.N. Ntainjua, A.F. Carley, A.A. Herzing, C.J. Kiely, G.J. Hutchings, Switching off hydrogen peroxide hydrogenation in the direct synthesis process, Science 323 (2009) 1037–1041.

[7] P. Centomo, C. Meneghini, S. Sterchele, A. Trapananti, G. Aquilanti, M. Zecca, In situ X-ray absorption fine structure spectroscopy of a palladium catalyst for the direct synthesis of hydrogen peroxide: leaching and reduction of the metal phase in the presence of bromide ions, ChemCatChem 7 (2015) 3712–3718.

[8] Y.F. Han, Z. Zhong, K. Ramesh, F. Chen, L. Chen, T. White, Q. Tay, S.N. Yaakub, Z. Wang, Au promotional effects on the synthesis of $H_2O_2$ directly from $H_2$ and $O_2$ on supported Pd–Au alloy catalysts, J. Phys. Chem. C 111 (2007) 8410–8413.

[9] S. Maity, M. Eswaramoorthy, Ni–Pd bimetallic catalysts for the direct synthesis of $H_2O_2$ – unusual enhancement of Pd activity in the presence of Ni, J. Mater. Chem. A 4 (2016) 3233–3237.

[10] D.A. Crole, R. Underhill, J.K. Edwards, G. Shaw, S.J. Freakley, G.J. Hutchings, R.J. Lewis, The Direct Synthesis of Hydrogen Peroxide from $H_2$ and $O_2$ using Pd-Ni/$TiO_2$ Catalysts, Phil. Trans. R. Soc. A. 378 (2020) 20200062.

[11] S.J. Freakley, Q. He, J.H. Harrhy, L. Lu, D.A. Crole, D.J. Morgan, E.N. Ntainjua, J.K. Edwards, A.F. Carley, A.Y. Borisevich, C.J. Kiely, G.J. Hutchings, Palladium-tin catalysts for the direct synthesis of $H_2O_2$ with high selectivity, Science 351 (2016) 965–968.

[12] F. Menegazzo, M. Signoretto, E. Ghedini, G. Strukul, Looking for the "dream catalyst" for hydrogen peroxide production from hydrogen and oxygen, Catalysts 9 (2019) 251.

[13] S. Ranganathan, V. Sieber, Recent advances in the direct synthesis of hydrogen peroxide using chemical catalysis—a review, Catalysts 8 (2018) 379.

[14] K. Kusada, H. Kobayashi, R. Ikeda, Y. Kubota, M. Takata, S. Toh, T. Yamamoto, S. Matsumura, N. Sumi, K. Sato, K. Nagaoka, H. Kitagawa, Solid solution alloy nanoparticles of immiscible Pd and Ru elements neighboring on Rh: changeover of the thermodynamic behavior for hydrogen storage and enhanced CO-oxidizing ability, J. Am. Chem. Soc. 136 (2014) 1864–1871.

[15] H. Kobayashi, H. Morita, M. Yamauchi, R. Ikeda, H. Kitagawa, Y. Kubota, K. Kato, M. Takata, S. Toh, S. Matsumura, Nanosize-induced drastic drop in equilibrium hydrogen pressure for hydride formation and structural stabilization in Pd–Rh solid-solution alloys, J. Am. Chem. Soc. 134 (2012) 12390–12393.

[16] Y. Vasquez, Z. Luo, R.E. Schaak, Low-temperature solution synthesis of the non-equilibrium ordered intermetallic compounds $Au_3Fe$, $Au_3Co$, and $Au_3Ni$ as nanocrystals, J. Am. Chem. Soc. 130 (2008) 11866–11867.

[17] T. Komatsu, H. Kobayashi, K. Kusada, Y. Kubota, M. Takata, T. Yamamoto, S. Matsumura, K. Sato, K. Nagaoka, H. Kitagawa, First-principles calculation, synthesis,

and catalytic properties of Rh-Cu alloy nanoparticles, Chem. Eur. J. 23 (2017) 57–60.

[18] B. Huang, H. Kobayashi, T. Yamamoto, S. Matsumura, Y. Nishida, K. Sato, K. Nagaoka, S. Kawaguchi, Y. Kubota, H. Kitagawa, Solid-solution alloying of immiscible Ru and Cu with enhanced CO oxidation activity, J. Am. Chem. Soc. 139 (2017) 4643–4646.

[19] K. Kusada, M. Yamauchi, H. Kobayashi, H. Kitagawa, Y. Kubota, Hydrogen-storage properties of solid-solution alloys of immiscible neighboring elements with Pd, J. Am. Chem. Soc. 132 (2010) 15896–15898.

[20] J. Li, T. Ishihara, K. Yoshizawa, Theoretical revisit of the direct synthesis of $H_2O_2$ on Pd and Au@Pd surfaces: a comprehensive mechanistic study, J. Phys. Chem. C 115 (2011) 25359–25367.

[21] Y. Xu, M. Mavrikakis, Adsorption and dissociation of $O_2$ on gold surfaces: effect of steps and strain, J. Phys. Chem. B 107 (2003) 9298–9307.

[22] D.H. Seo, H. Shin, K. Kang, H. Kim, S.S. Han, First-principles design of hydrogen dissociation catalysts based on isoelectronic metal solid solutions, J. Phys. Chem. Lett. 5 (2014) 1819–1824.

[23] K.P. de Jong, in: Synthesis of Solid Catalysts, Wiley, 2009, pp. 59–82.

[24] G. Kresse, J. Furthmüller, Efficiency of ab-initio total energy calculations for metals and semiconductors using a plane-wave basis set, J. Comput. Mater. Sci. 6 (1996) 15–50.

[25] G. Kresse, D. Joubert, From ultrasoft pseudopotentials to the projector augmented-wave method, Phys. Rev. B 59 (1999) 1758–1775.

[26] B. Hammer, L.B. Hansen, J.K. Nørskov, Improved adsorption energetics within density-functional theory using revised Perdew-Burke-Ernzerhof functionals, Phys. Rev. B 59 (1999) 7413–7421.

[27] D. Sheppard, R. Terrell, G. Henkelman, Optimization methods for finding minimum energy paths, J. Chem. Phys. 128 (2008) 134106.

[28] Y. Yamauchi, A. Tonegawa, M. Komatsu, H. Wang, L. Wang, Y. Nemoto, N. Suzuki, K. Kuroda, Electrochemical synthesis of mesoporous Pt–Au binary alloys with tunable compositions for enhancement of electrochemical performance, J. Am. Chem. Soc. 134 (2012) 100–5109.

[29] Y. Kim, H.J. Kim, Y.S. Kim, S.M. Choi, M.H. Seo, W.B. Kim, Shape- and composition-sensitive activity of Pt and PtAu catalysts for formic acid electrooxidation, J. Phys. Chem. C 116 (2012) 18093–18100.

[30] C. Guo, M. Zhang, H. Tian, T. Wang, J. Hu, Preparation and enhanced catalytic activity of Pt-Au alloy catalysts for formic acid oxidation, J. Electrochem. Soc. 160 (2013) F1187–F1191.

[31] D. Wang, X. Cui, Q. Xiao, Y. Hu, Z. Wang, Y.M. Yiu, T.K. Sham, Electronic behaviour of Au-Pt alloys and the 4f binding energy shift anomaly in Au bimetallics - X-ray spectroscopy studies, AIP Adv. 8 (2018) 065210.

[32] N.M. Wilson, P. Priyadarshini, S. Kunz, D.W. Flaherty, Direct synthesis of $H_2O_2$ on Pd and $Au_xPd_1$ clusters: understanding the effects of alloying Pd with Au, J. Catal. 357 (2018) 163–175.

[33] From KITCO website, the prices of Pd, Pt, and Au are \$75.8, \$23.3, and \$51.8 per gram (g), respectively. https://www.kitco.com/charts/, 2020 (accessed 25 March 2020).

[34] R.B. Rankin, J. Greeley, Trends in selective hydrogen peroxide production on transition metal surfaces from first principles, ACS Catal. 2 (2012) 2664–2672.

[35] C. Samanta, Direct synthesis of hydrogen peroxide from hydrogen and oxygen: an overview of recent developments in the process, Appl. Catal. A-Gen. 350 (2008) 133–149.

[36] R.J. Lewis, G.J. Hutchings, Recent advances in the direct synthesis of $H_2O_2$, ChemCatChem 11 (2019) 298–308.

[37] A. Plauck, E.E. Stangland, J.A. Dumesic, M. Mavrikakis, Active sites and mechanisms for $H_2O_2$ decomposition over Pd catalysts, Proc. Natl. Acad. Sci. U.S.A. 113 (2016) E1973–E1982.